# DEFECT-AWARE PHYSICS-BASED COMPACT MODEL FOR FERROELECTRIC NVCAP: FROM TCAD CALIBRATION TO CIRCUIT CO-DESIGN

#### A PREPRINT

Luca Fehlings\*¹, Nihal Raut ², ◎ Md. Hanif Ali², ◎ Francesco M. Puglisi³, ◎ Andrea Padovani⁴, ◎ Veeresh Deshpande², and ◎ Erika Covi¹

<sup>1</sup>Zernike Institute for Advanced Materials and CogniGron, University of Groningen
 <sup>2</sup>Department of Electrical Engineering, Indian Institute of Technology Bombay
 <sup>3</sup>Department of Engineering "Enzo Ferrari", University of Modena and Reggio Emilia
 <sup>4</sup>Department of Engineering Sciences and Methods, University of Modena and Reggio Emilia

November 27, 2025

#### ABSTRACT

Ferroelectric non-volatile capacitance-based memories enable non-destructive readout and low-power in-memory computing with 3D stacking potential. However, their limited memory window (1-10 fF/ $\mu$ m²) requires material-device-circuit co-optimization. Existing compact models fail to capture the physics of small-signal capacitance, device variability, and cycling degradation, which are critical parameters for circuit design. In non-volatile capacitance devices, the small-signal capacitance difference of the polarization states is the key metric. The majority of the reported compact models do not incorporate any physical model of the capacitance as a function of voltage and polarization. We present a physics-based compact model that captures small-signal capacitance, interface and bulk defect contributions, and device variations through multi-scale modeling combining experimental data, TCAD simulations, and circuit validation. Based on this methodology, we show optimized memory read-out with  $\pm 5$  mV sense margin and impact of device endurance at the circuit level. This work presents a comprehensive compact model which enables the design of selector-less arrays and 3D-stacked memories for compute-in-memory and storage memory.

# 1 Introduction

Ferroelectric technology has emerged as a promising low-power alternative to conventional complementary metal oxide semiconductor (CMOS) solutions for storage memory and compute-in-memory (CIM) applications. Recent research focuses on exploring non-destructive read methodologies through non-volatile capacitor (nvCap) devices. The built-in electric field in the ferroelectric capacitor results in the presence of a non-volatile small-signal capacitance that depends on the polarization of the ferroelectric, determining a high-capacitance state (HCS) and low-capacitance state (LCS) [1, 2]. This phenomenon, often modeled as a polarization-dependent dielectric constant, facilitates the non-destructive read functionality. Electronic mechanisms cause this capacitance hysteresis, as demonstrated by GHz-regime impedance measurements [3], enabling high-speed read operations. Further, the capacitance can be read with voltages well below the coercive voltage of the device and a low read-disturb [4], while maintaining the low-voltage program and erase operations of a ferroelectric capacitor (FeCap). The nvCap device offers the possibility of selector-less or one transistor, one capacitor (1T1C) memory arrays and 3D stacking [5] for high-density memory (Fig. 1). However, nvCap devices have a limited memory window (1-10 fF/µm²) and the read signal is severely limited by the bit line capacitance [6]. While material stacks optimized for nvCap operation are already being researched [7], there is a need for careful co-design of the material stack, devices, and memory circuit to ensure reliability and performance. Therefore, it is necessary to develop a physics-based compact model that incorporates the key material and device physics to allow

<sup>\*</sup>Corresponding author: l.d.fehlings@rug.nl

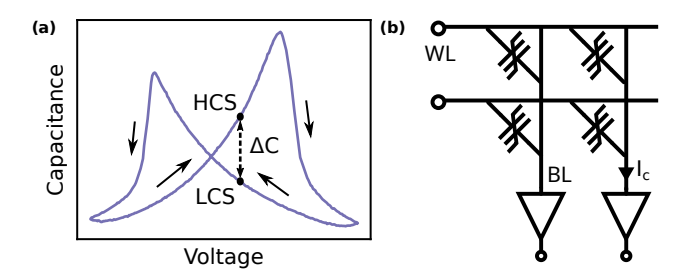


Figure 1: (a) Illustration of the nvCap capacitance and polarization hysteresis. A capacitive memory window  $\Delta C$  can be extracted as difference between the HCS and the LCS. (b) Possible application in a selector-less crossbar array enabled by the capacitive nature of the memory device.

reliable circuit design as well as Monte Carlo, post-layout and noise verification. Further, critical device and material parameters need to be identified to enable design-technology co-optimization (DTCO) to overcome the low signal amplitude particularly for high bit line capacitances in large arrays. Conventional ferroelectric capacitor models [8, 9, 10, 11, 12, 13] cannot support design flows that require device-circuit co-optimization with reliability, aging, noise, and mismatch. These models have three critical limitations: (1) they lack self-consistent and physics-based small-signal capacitance modeling, (2) they ignore device-to-device variations, (3) they ignore defects and related degradation mechanisms and (4) they cannot be calibrated with TCAD simulations. Technology computer-aided design (TCAD) simulations are critical for the vertication and the calibration of compact models, in particular for parameters that are difficult to observe directly, such as defects. As a result of these shortcomings, the design and optimization of the circuits needed to read and program these devices is challenging. In this study, we propose a DTCO framework based on experimental data, TCAD simulations, and a VerilogA compact model. This approach extends an existing compact model by a interface-defect-based capacitance and a bulk-defect-based leakage current model. Therefore, the model can be verified by TCAD simulations in addition to experimental data, and DTCO can be performed by providing a comprehensive link between the extracted defect parameters and the electrical behavior. Based on this, we present a read-circuit that produces a 10 mV memory window at the bit line, showing the need for sub-mV offset-calibrated sense amplifiers and aggressive bit line capacitance reduction for reliable and degradation-aware memory designs.

## 2 Device Fabrication and Characterization

We demonstrate our framework using W-Al $_2$ O $_3$ -Hf $_{0.5}$ Zr $_{0.5}$ O $_2$ -W bi-layer capacitors (Fig. 2). The presence of asymmetric interfaces gives rise to an in-built electric field in the device at 0 bias, leading to a non-volatile capacitance. The stack (Fig. 2(a)) comprises a 50 nm sputtered W bottom electrode, 2 nm Al $_2$ O $_3$ , and 10 nm HZO layers (ALD at 200°C), and a 50 nm sputtered W top electrode. The device measures 100 µm  $\times$  100 µm. Post-metallization annealing was carried out at 450°C for 720 s in a nitrogen (N $_2$ ) environment. The nvCap devices are woken up with 1 k cycles at 1 kHz. Small signal capacitance-voltage (CV) measurements are performed with quasi-static DC voltage sweep combined with small AC signal of 30 mV amplitude.

# 3 Material-Device-Circuit Co-design Methodology

We demonstrate a co-design methodology integrating experimental data, TCAD simulations for defect density extraction, a physics-based compact model, and read circuit validation with both the nvCap compact model and a CMOS PDK. The experimental data from a bilayer stack nvCap device (Fig. 2(a) are used to calibrate the compact model for ferroelectric and interface layer parameters. Furthermore, the leakage current data is reproduced in the Ginestra<sup>TM</sup> semiconductor device simulation TCAD [14] to characterize the behavior and extract trap properties. We then incorporate these trap properties (Fig. 2(b)) in the compact model (Fig. 2(c)). This includes the trap density  $N_{tr,fe}$  for the bulk leakage current, based on the trap-assisted tunneling (TAT) conduction mechanism. The interface trap properties  $N_{tr,depl\uparrow/\downarrow}$  are extrapolated from this bulk density and are calibrated against the experimental CV hysteresis. The effects of these interface defects are treated in the compact model as contributions to polarization screening and are therefore grouped together at the interface. However, they do not necessarily represent defects located exactly at the material interface; defects throughout the material stack can influence polarization screening and bias behavior.

A schematic of the segments and physics included in the compact model for nvCap is presented in Fig. 2(b-c). The ferroelectric device model is based on our previous work [15], which calculates a self-consistent solution based on

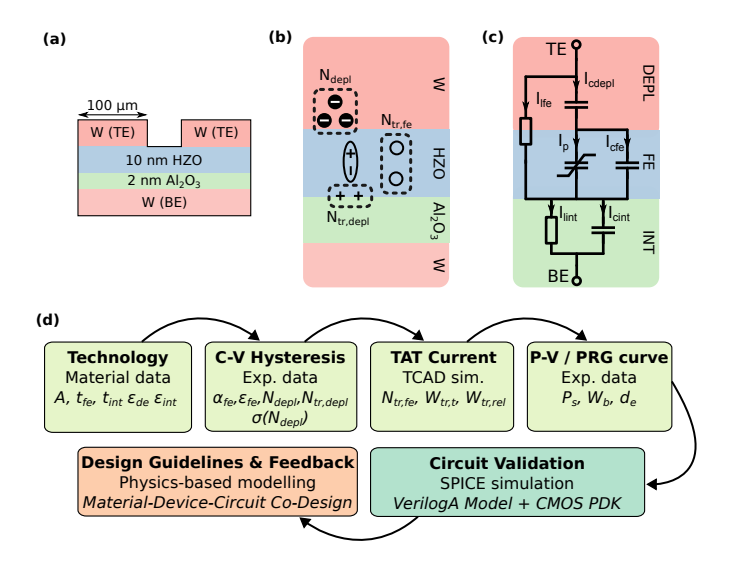


Figure 2: (a) Material stack of the fabricated nvCap devices. (b) The nvCap device behavior is impacted by non-idealities, such as the carrier density at the electrode interface leading to finite screening, bulk traps in the HZO causing leakage currents and interface traps that screen the polarization, circumventing depolarization effects from finite screening due to the electrode depletion and interface layer. (c) Equivalent circuit that models the ferroelectric switching and its interaction with the depletion effect, interface layer and leakage currents self-consistently. (d) Calibration flow with the parameters extracted in each step. The calibration is based on technology data, electrical characterization data and TCAD simulations, leading to a physics-based VerilogA compact model that enables material-device-circuit co-design by circuit validation and design feedback.

contributions from the ferroelectric, interface and electrode layers. In order to provide an accurate description of the non-volatile small-signal capacitance, it is necessary to incorporate interface and bulk defects into the model. In this model (Fig. 2(b)), we consider the contribution of finite screening charges  $N_{depl}$  in the electrode interface, bulk defects  $N_{tr,fe}$  within the ferroelectric for leakage currents, static interface trap charges  $N_{tr,depl}$  that contribute to the capacitance hysteresis and dynamic interface charges  $(I_{lfe} - I_{lint})dt$  that contribute to the ferroelectric polarization screening.

Therefore, we present a compact model that includes the reliability of aging of ferroelectric devices, enabling the optimization of circuits for predictive design through a multiscale modeling approach. We model leakage currents through trap-assisted tunneling (TAT) [16]. This VerilogA implementation integrates with our existing device model and assumes single-tunnel events for thin films:

$$J_{tat} = \frac{q \cdot N_{tr,fe} \cdot x_c}{2\tau_c},\tag{1}$$

where  $N_{tr,fe}$  is the bulk trap density in the ferroelectric,  $x_c$  is the characteristic length where the tunneling current is maximized and  $\tau_c$  is the time constant of the capture process. In this approximation, the current density is linear with the trap density, which is plausible for thin films with a single tunnel event. For films on the order of 10 nm and thicker, where the TAT mechanism may involve multiple consecutive tunneling events for a charge to traverse the insulator, causing the current density to be super-linear with the defect density. The voltage-dependence of the current is given by the capture time constant calculated as in [16] in the framework of the multi-phonon theory [17]:

$$\tau_c^{-1} = c_0 N_c \exp\left(-\frac{x_{tm}}{\lambda_c}\right) \exp\left(-\frac{E_{c,j}}{k_B T}\right),\tag{2}$$

with trap-specific constant  $c_0$ , conduction band density of states  $N_c$ , characteristic tunneling length for the capture process  $\lambda_c$ , thermal activation barrier for the capture process  $E_{c,j}$ , Boltzmann constant  $k_B$  and temperature T. The characteristic distance  $x_{tm}$  represents the trap position where the tunneling current maximizes. This position depends on the applied voltage, film thickness, and trap energy level relative to the conduction band.

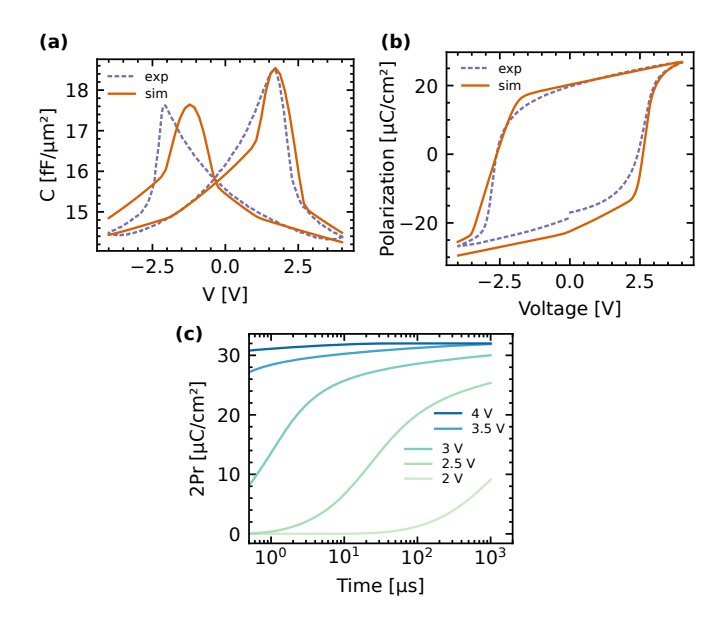


Figure 3: (a) Capacitance vs Voltage curve using quasi-static voltage sweep after 1000 wake-up cycles and compact model fit with the experimental curve. (b) Polarization vs Voltage curve after 1000 wake-up cycles using PUND sequence of 1 kHz and fit of the compact model with the experimental curve. (c) Compact model simulation of the switching kinetics towards the down polarization state showing the transient programming behavior.

$$x_{tm} = \frac{A \cdot \left(\sqrt{\frac{B \cdot V_{fe}^2}{V_t} + \frac{C \cdot V_{fe}}{V_t} + 4t_{fe}^2} - 2At_{fe} + DV_{fe}\right)}{\lambda_c \cdot QV_{fe}^2},$$
(3)

$$A = 2 \cdot E_{tr,rel} \cdot t_{fe} \cdot k_B \cdot T, \tag{4}$$

$$B = \frac{\lambda \cdot t_{fe}}{E_{tr,rel}} + \frac{\lambda_c^2}{4V_t},\tag{5}$$

$$C = \frac{\lambda_c \cdot t_{fe} \cdot (E_{tr,t} - E_{tr,rel} - \phi_{b,fe})}{E_{tr,rel}},$$
(6)

$$D = \lambda_c \cdot t_{fe} \cdot P_Q \cdot (\phi_{b,fe} - E_{tr,t} + E_{tr,rel}), \tag{7}$$

with applied voltage  $V_{fe}$ , thermal voltage  $V_t$ , layer thickness  $t_{fe}$ , elementary charge q, trap's relaxation  $E_{tr,rel}$ , and thermal ionization  $E_{tr,t}$  energies, cathode to insulator barrier  $\phi_{b,fe}$ . The characteristic tunnel length is given by

$$\lambda_c = 2\sqrt{\phi_{b,fe} 2m^* q/\hbar^2},\tag{8}$$

with the electron effective mass in the insulator  $m^*$  and reduced Planck constant  $\hbar$ . The thermal activation barrier for the multi-phonon capture process is calculated via

$$E_{c,j} = (E_{tr,rel} - \Delta E_j)^2 / (4E_{tr,rel}),$$
 (9)

$$\Delta E_i = E_{tr,t} + V_{fe} x_{tm} / t_{fe} - \phi_{b,fe}. \tag{10}$$

Elaborations on and the derivation of this TAT compact model can be found in the original publication [16].

We model capacitance hysteresis using a voltage-dependent series capacitance that accounts for incomplete screening at the metal electrodes. This capacitance depends on both voltage and polarization state. This capacitance is calculated independently for the up- and down-polarized domains:

$$C_{depl\downarrow/\uparrow} = \frac{\varepsilon_{depl}qN_{depl}}{\varepsilon_{fe}E_{fe} \pm (P_s - qN_{tr,depl\downarrow/\uparrow})},$$
(11)

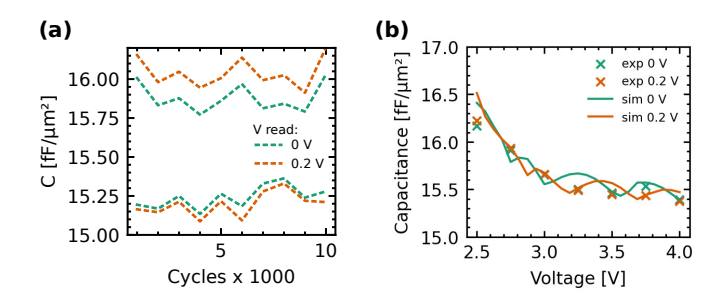


Figure 4: (a) Capacitance vs Cycles measured using quasi-static voltage sweep from 0 V to 200 mV after every 1000 cycles. (b) Erasing obtained by applying incrementally positive polarity pulse amplitudes, capacitance measured at DC 0 V and 0.2 V, and fit of the compact model with the experimental curve.

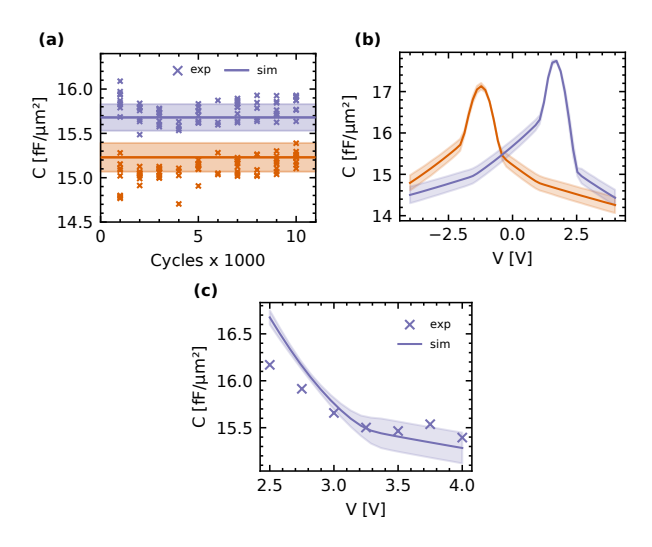


Figure 5: (a) Capacitance measured at 0 V over cycles (crosses) and compact model Monte Carlo simulation of the LCS and HCS capacitance with mean and  $3 \sigma$ . (b) Compact model Monte Carlo simulation of the capacitance hysteresis with mean and  $3 \sigma$  indicated. (c) Programming curve of the HCS, measured at 0 V, and the respective compact model Monte Carlo simulation with mean and  $3 \sigma$ .

with polarizability  $\varepsilon_{depl}$ , carrier density  $N_{depl}$ , permittivity of the ferroelectric layer  $\varepsilon_{fe}$ , saturation polarization  $P_s$  and trap densities for the respective polarity  $N_{tr,depl\downarrow/\uparrow}$ . The total capacitance is then proportional to the fraction of up- and down-polarized domains:

$$C_{depl} = p \cdot C_{depl\downarrow} + (1 - p) \cdot C_{depl\uparrow}, \tag{12}$$

with polarization p normalized between 0 (up) and 1 (down). This models two parallel capacitors  $C_{depl\downarrow/\uparrow}$  which are voltage-dependent, and where each contribution to the total capacitance is dependent on the polarization. The characteristic peaks in the capacitance hysteresis then arise from the gradual transition from one capacitance to the other, where both capacitances have opposing voltage dependencies. In addition, the model considers non-polar phases within the hafnium zirconium oxide (Hf $_{0.5}$ Zr $_{0.5}$ O $_{2}$ ) (HZO) layer, i.e. a monoclinic phase portion, that are modeled as a capacitance in parallel to that of the polar, ferroelectric contributions. The relative phase portion  $\alpha_{fe}$  of the ferroelectric phase and the permittivity  $\varepsilon_{de}$  of the dielectric phase then shift the observed capacitance hysteresis up or down, while leaving the qualitative shape unchanged.

The experimentally calibrated compact model is then utilized for circuit simulations along with commercial foundry CMOS process design kit (PDK) to show its application in realistic circuit design.

# 4 Parameter Extraction & Model Calibration

In our framework, we follow a hierarchical parameter extraction and model calibration procedure (Fig. 2(d)) that draws from experimental characterization, TCAD simulations and literature on material characterization and simulation.

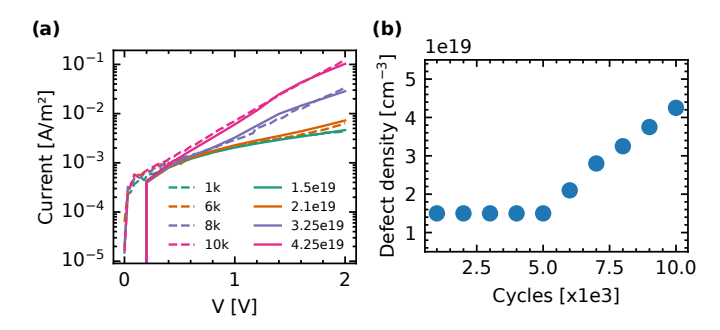


Figure 6: (a) Comparison of the simulated and experimental curve of leakage vs cycles for defect level estimation using Ginestra. The leakage current < 500 mV is only minimally affected by increasing defects. (b) Defect densities extracted from the Ginestra fitting. For low cycles the extracted defect density is constant as the leakage current is dominated by resistive current.

Geometric parameters, such as the area and the layer thicknesses are based on the physical characterization or design of the device and material deposition processes. This also extends to material parameters such as the dielectric constants of the hafnia (HfO<sub>2</sub>) and alumina (Al<sub>2</sub>O<sub>3</sub>) layers, where small variations can be imposed to fit the model. Then, parameters are extracted from the C-V hysteresis. The base capacitance, reflected by the linear capacitors  $I_{cfe}$  and  $I_{cint}$ , is governed by the dielectric constants of the materials  $\varepsilon_{fe}$ ,  $\varepsilon_{de}$  and  $\varepsilon_{int}$ , as well as the fraction of polar domains in the ferroelectric  $\alpha_{fe}$ . The capacitance peak is then governed by the non-linear depletion capacitance  $I_{cdepl}$ , where the carrier density  $N_{depl}$  modulates the amplitude of the peak. The interface trap charges  $N_{tr,depl\downarrow\uparrow\uparrow}$  then result in an asymmetry in the peak heights and the built-in bias, where a higher difference between the trap densities for the two polarities leads to a higher peak asymmetry and built-in bias. This also translates to the built-in bias seen in the P-V hysteresis. Then, the parameters of the tunneling/leakage currents are extracted from quasi-static leakage current measurements. Here, TCAD simulations that reproduce the leakage currents are employed to extract trap properties, such as the trapping site density  $N_{tr,fe}$  and the trap energy levels  $W_{tr,t}$  and  $W_{tr,rel}$ , to ensure physicality and generality of the parameters. For the calibration of the switching parameters we refer to the compact model this framework is based on [15], where the switching model and the calibration of its parameters are explained in detail. For any of these steps in the calibration process, the parameters can be assigned a distribution in addition to the mean value to model mismatch or process variations. The parameters extracted using the framework for the compact model are listed in Table 1.

#### 5 Results and Discussion

Our simulation program with integrated circuit emphasis (SPICE) compact model uses a polarization switching mechanism modulated by depolarization fields from electrode depletion and interface layers [15]. An initial calibration of the model is carried out by extracting its parameters from experimental electrical characterization data. For this, the CV measurement is taken as main calibration target and other measurements are used to confirm that the compact model generalizes the device behavior. This quasi-static CV measurement post wake-up is shown in Fig. 3(a) together with the simulation from the compact model. The model captures the CV curve closely, particularly for positive voltages, and is able to reproduce the asymmetry observed in the experimental curve. In particular, the asymmetry in the CV peak amplitudes and the voltage bias are dictated by the interface charge density  $N_{tr,depl\downarrow/\uparrow}$ . These interface charges screen the polarization dipoles, i.e. the higher these charge densities are, the less the influence of the respective polarization dipoles on the depletion capacitance and therefore the CV hysteresis. These parameters also reproduce the experimental P-V hysteresis loop (Fig. 3(b)), as well as the switching kinetics for the erase state, illustrated in Fig. 3(c). This result demonstrates consistency in the prediction of small-signal and large-signal behavior.

Figure 4(a) shows the capacitance versus cycling for high and low capacitance states at 0 V and 0.2 V read bias. The memory window increases only marginally at 0.2 V because the built-in field from the asymmetric stack creates a memory window at zero bias. This built-in field simplifies the read circuit design by eliminating the need for a bias voltage. Erase measurements are shown in Fig. 4(b) and were obtained after 1 k cycles through the initialization of the nvCap in the program state, followed by the application of erase pulses with magnitudes ranging from 2.5 V to 4 V in steps of 0.25 V. The model accurately captures the gradual erase process at both voltages.

Furthermore, the capacitive memory window was verified at 0 V and 200 mV read voltages after every 1000 programming cycles of  $\pm 4$  V/1 ms (Fig. 5(a)), and the variability of the LCS and HCS was extracted from the measurement. This variability was then included in the compact model by a variation of  $n_{depl}$  with a standard deviation of  $3.9 \cdot 10^{20} cm^{-3}$ ,

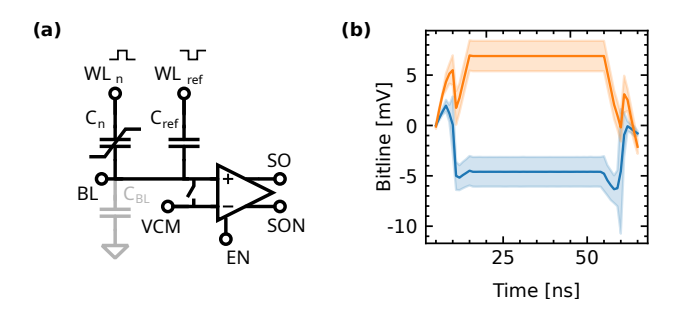


Figure 7: (a) In the digital memory macro, the currents of the nvCap and of the reference capacitor are summed up on the BL capacitance. (a) Monte Carlo circuit simulation in a commercial CMOS PDK with the nvCap compact model showing the voltage on the BL during a 40 ns read operation for LCS and HCS with 3  $\sigma$ .

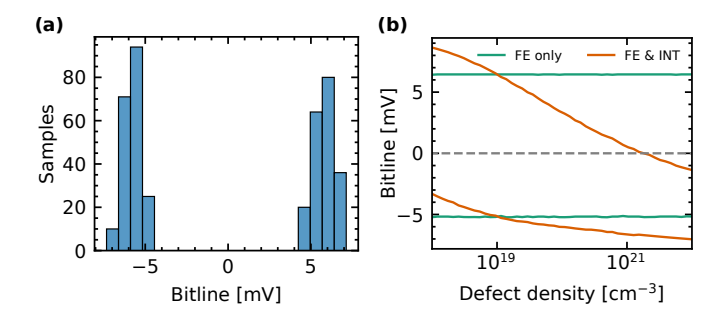


Figure 8: (a) Histogram of the BL potential for LCS and HCS states in the Monte Carlo circuit simulation. (b) Circuit simulation showing BL signal degradation due to increasing bulk defects (in the FE only and in both FE and INT) during endurance cycling. As the leakage current < 500 mV is dominated by the interface, the FE defects and leakage alone have limited influence on the signal.

which models the variability in charge screening by the electrodes, to match mean and standard deviation of the measured memory windows. A Monte Carlo simulation of the CV hysteresis with these variability parameters as shown in Fig. 5(b), is used to select a suitable a read voltage for a robust read operation. The calibration reveals that, within the model, the variability of the capacitance is lowest at the peaks and increases the farther the bias is away from the peaks. The model accurately captures the erase process, as demonstrated in Fig. 5(c), in conjunction with the experimental data. The Monte Carlo simulation also predicts a larger spread for HCS with a higher erase voltage, which is in accordance with the increase seen in Fig. 5(c).

Endurance cycling results in the degradation of the nvCap, exhibiting a comparable effect to that of device aging. Device endurance directly impacts circuit reliability. We now demonstrate how cycling-induced defect generation affects both leakage current and read margin. This analysis enables circuit designers to set refresh requirements and error correction overhead. In order to extract defect density from devices, we used the Ginestra<sup>TM</sup> software to reproduce experimental leakage current density data versus cycles for the erase state (Fig. 6(a)). These TCAD-extracted defect densities then parameterize the compact model's TAT mechanism (Eqs. 1–10). The results indicate an increase in leakage, attributable to an increase of the defect density resulting from cycling (Fig 6(b)). The findings from the Ginestra analysis are incorporated within the compact model through the implementation of a trap-assisted tunneling model [16, 17]. This linkage enables predictive modeling: changes in process conditions that alter defect density can be simulated at the circuit level without re-extracting the full compact model. The degradation analysis requires the estimation of the trap density changes with cycling. The impact on small-signal CV is illustrated in Fig. 9(a) for various interface defect densities. As previously observed, the non-volatile capacitance (at 0 V) exhibits a substantial dependency on interface trap density.

The compact model is then employed to design and size a digital read-out macro, as in Fig. 7. The sense amplifier (SA, Fig. 7(a)) is a latch with a differential pair input [4]. All following BL and word line (WL) voltages described here are relative to the common mode voltage that the BL is pre-charged to. The circuit's operating principle entails the application of a 300 mV read pulse, which induces a change in the charge on the positive input of the SA, proportional to the capacitance of the FeCap. This charge is added to the charge originating from a reference capacitor  $C_{ref}$ , normalizing the LCS and HCS voltages around 0. Consequently, this results in a change in voltage on the BL (Fig. 9(b)),

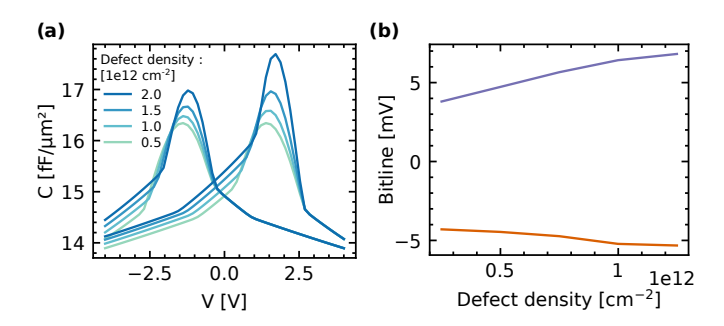


Figure 9: (a) Simulation of the compact model capacitance hysteresis as a function of interface defects for the up polarization state that act as trapping and polarization screening sites. (b) Circuit simulation of the BL signal as a function of the interface defects for the up polarization state. The interface modulates the polarization screening by trapped charges and hence the capacitive memory window (cf. Fig. 5(a)).

which is pre-charged to a common-mode voltage  $V_{cm}$  and is amplified by the latch. We performed Monte Carlo simulations including nvCap variability, CMOS transistor mismatch, and process variations. Figure 8(a) demonstrates that a minimum sense margin of  $\pm 5$  mV can be achieved. The read yield, defined as the number of correct bit read-out divided by the number of Monte Carlo simulations carried out, for bit 0 is shown in Fig. 7(c). Our model demonstrates inclusion of variability, aging and ability to co-design with CMOS for the purpose of achieving optimal read margin.

The impact of increasing of trapped charges originating from interface defects on the up polarization state in the nvCap capacitance hysteresis is illustrated in Fig. 9(a). The trapped charges for the down polarization state are kept constant at  $5 \cdot 10^{11} \ cm^{-2}$ . The capacitive memory window increases with the number of defects, as well as the asymmetry between positive and negative voltage portions of the hysteresis. As the number of interface defects increases for the up polarization state, the capacitive memory window increases due to better polarization screening (Eq. 11). Fig. 9(b) shows the respective impact on the BL voltage, where an increase in the aforementioned capacitive memory window translates to an increase in the BL voltage for increasing defects. The combination of bulk defects in the ferroelectric and dielectric interface layer leads to a degradation of the signal on the BL, as shown in Fig. 8(b), due to higher leakage currents. Bulk defects in the ferroelectric layer alone do not significantly impact the read margin in our simulation. This is due to the leakage current being dominated by the interface contribution for voltages below 500 mV in the compact model simulation, as the voltage drop over the interface dominates over the ferroelectric in that regime. This is in accordance with the experimental and TCAD simulation in Fig. 6(a), where currents below 500 mV show little dependence on defect density in the ferroelectric. An input offset of the sense amplifer of less than  $\pm 5$  mV is required when defects increase above  $10^{21}/\text{cm}^3$ .

Based on the analysis done with our framework, we derive the following device and circuit design guidelines: Due to the low capacitive memory window, particularly for devices with scaled area, there is a strong tradeoff in device area, bit line capacitance, read voltage and sense amplifier. In particular for larger arrays and under the consideration of noise, device and circuit have to undergo in-depth co-design. To increase the available capacitive memory window, our framework suggests a strong asymmetry between interface charges for the up and down polarization directions. This comes, however, at the cost of an increase built-in bias, potentially increasing program and erase voltages, and could pose reliability challenges. The variability in the capacitive memory window and read-out yield shows a strong dependence on the electrode screening properties, with a variation in the carrier density  $n_{depl}$  showing large read signal variability. An optimization of the yield then requires strong control of the electrode interface on the device side and offset compensation below a few millivolts for the sense amplifier. Bulk traps, especially for the dielectric  $Al_2O_3$  layer, contribute severely to the leakage current, and an increase during the devices life-cycle shows a decrease in the bit line signal for increasing defects. The device therefore needs to be optimized to limit defects that participate in trap-assisted tunneling to limit the decrease in bit line signal during aging.

### 6 Conclusion

We propose a material-device-circuit co-design framework for developing a non-destructive read-out of nvCap. This framework is based on experimental characterization of a bi-layer nvCap device, kinetic Monte Carlo-based TCAD simulations and a physics-based compact model. The proposed compact model has the capacity to replicate the behavior of the nvCap including the modeling of defect contributions to the capacitance hysteresis and leakage currents. It further allows to extract device variability to model process variability and mismatch. These results are then applied to a memory circuit where sense margins are extracted based on variability and defect parameters. The defect-based modeling

Table 1: Model parameters

Parameter Value		Description
$\alpha_{fe}$	0.6	Fraction of ferroelectric do-
v		mains
$\varepsilon_{fe}$	70	Permittivity of ferroelectric do-
		mains
$\varepsilon_{de}$	20	Permittivity of dielectric do-
		mains
$\varepsilon_{depl}$	2.2	Polarizability electrode inter-
D	202	face
$P_s$	20 μC/cm <sup>2</sup>	Saturation polarization
$N_{depl}$	$1.2 \cdot 10^{22}  \mathrm{cm}^{-3}$	Carrier density electrode inter-
	20 0	face
$\sigma(N_{depl})$	$3.9 \cdot 10^{20} \text{ cm}^{-3}$	Std. dev. $n_{depl}$ (Monte Carlo
		only)
$N_{tr,depl\uparrow}$	0	Screening charge density P <sub>↑</sub>
$N_{tr,depl\downarrow}$	$7.5 \cdot 10^{13} \text{ cm}^{-2}$	Screening charge density P <sub>↓</sub>
$\varphi_{b,fe}$	2 eV	FE layer conduction band offset
$\varphi_{b,int}$	2.7 eV	INT layer conduction band off-
		set
$N_{tr,fe}$	$1.5 \cdot 10^{19}  \mathrm{cm}^{-3}$	Trap density in the FE
$m_{fe}^*$	0.4	Electron effective mass
$W_{tr,t}^{j}$	2.1 eV	Thermal ionization energy
$W_{tr,rel}$	1.19 eV	Relaxation energy
$x_c$	5 nm	Tunneling characteristic length
$c_0 N_c$	$1e-8 \text{ s}^{-1}$	Trap-specific constant

approach enables circuit designs that compensate for reliability and aging. This capability is essential for advanced storage and compute-in-memory applications where array size and endurance requirements challenge conventional design margins. By linking process and cycling-induced defects to circuit-level performance, this framework supports technology-circuit co-optimization from early process development through memory array design.

# Acknowledgment

The authors thank Gaurav Thareja and Luca Larcher from Applied Materials for their mentorship and access to the Ginestra<sup>TM</sup> proprietary simulation platform.

This work was supported by the European Research Council (ERC) through the European's Union Horizon Europe Research and Innovation Programme under Grant Agreement No 101042585. Views and opinions expressed are however those of the authors only and do not necessarily reflect those of the European Union or the European Research Council. Neither the European Union nor the granting authority can be held responsible for them. The University of Groningen would like to acknowledge the financial support of the CogniGron research center and the Ubbo Emmius Funds. IIT Bombay acknowledges funding from DST and MeitY through NNETRA project, iHUB DivyaSampark - IIT Roorkee. Support of IITBNF staff is acknowleged.

### References

- [1] S. Mukherjee, J. Bizindavyi, Y.-C. Luo, S. Clima, J. Read, M. I. Popovici, Y. Xiang, N. Bazzazian, A. Belmonte, R. Delhougne, G. S. Kar, F. Catthoor, V. V. Afanas'Ev, S. Yu, and J. Van Houdt, "Pulse-Based Capacitive Memory Window with High Non-Destructive Read Endurance in Fully BEOL Compatible Ferroelectric Capacitors," in 2023 International Electron Devices Meeting (IEDM), pp. 1–4, 2023.
- [2] O. Phadke, H. Mulaosmanovic, S. Dunkel, S. Beyer, and S. Yu, "Reliability Assessment of Ferroelectric nvCAP for Small-Signal Capacitive Read-Out," in 2024 IEEE International Reliability Physics Symposium (IRPS), pp. 1–5, IEEE, 2024.

- [3] T. Kim, E. R. Borujeny, I. Sardinero-Meirás, J. Grajal, K. C. Cadien, D. A. Antoniadis, and J. A. Del Alamo, "AC Impedance Characteristics of Ferroelectric Hf0.5Zr0.5O2: from 1 kHz to 10 GHz," in 2023 International Electron Devices Meeting (IEDM), pp. 1–4, 2023.
- [4] L. Fehlings, M. A. Chowdhury, B. S. Latibari, S. Salehi, and E. Covi, "Reliability of capacitive read in arrays of ferroelectric capacitors," in 2025 IEEE International Symposium on Circuits and Systems (ISCAS), pp. 1–5, IEEE, 2025.
- [5] N. Ramaswamy, A. Calderoni, J. Zahurak, G. Servalli, A. Chavan, S. Chhajed, M. Balakrishnan, M. Fischer, M. Hollander, D. P. Ettisserry, A. Liao, K. Karda, M. Jerry, M. Mariani, A. Visconti, B. R. Cook, B. D. Cook, D. Mills, A. Torsi, C. Mouli, E. Byers, M. Helm, S. Pawlowski, S. Shiratake, and N. Chandrasekaran, "NVDRAM: A 32Gb Dual Layer 3D Stacked Non-volatile Ferroelectric Memory with Near-DRAM Performance for Demanding AI Workloads," in 2023 International Electron Devices Meeting (IEDM), pp. 1–4, 2023.
- [6] Y. Xiang, S. Mukherjee, G. Hellings, H. Oh, M. G. Bardon, and J. Van Houdt, "Compact Modeling and Design Exploration of Non-Destructive Read-Out 1T1C FeRAM," *IEEE Transactions on Electron Devices*, 2024.
- [7] Z.-Y. Huang, H.-Y. Zhu, L. Shen, X.-X. Li, Z.-Y. Huang, Y.-C. Li, M. Li, R. Huang, D. W. Zhang, and H.-L. Lu, "Large capacitive memory window achieved in ferroelectric hzo capacitor with nbo x insertion layer for non-destructive read," *IEEE Electron Device Letters*, 2025.
- [8] C.-T. Tung, G. Pahwa, S. Salahuddin, and C. Hu, "A compact model of polycrystalline ferroelectric capacitor," *I.E.E.E. transactions on electron devices/IEEE transactions on electron devices*, vol. 68, pp. 5311–5314, 10 2021.
- [9] Z.-Y. Yan, R. Zhao, Z. Wang, T. Lu, H. Liu, K.-H. Xue, X. Miao, Y. Yang, and T.-L. Ren, "A Liouville Model for Polycrystalline Ferroelectrics Emphasizing Kinetic Integrity and Deployability in Circuits with Charge and Current Constraints," in 2023 International Electron Devices Meeting (IEDM), 12 2023.
- [10] M. Pešić, C. Künneth, M. Hoffmann, H. Mulaosmanovic, S. Müller, E. T. Breyer, U. Schroeder, A. Kersch, T. Mikolajick, and S. Slesazeck, "A computational study of hafnia-based ferroelectric memories: from ab initio via physical modeling to circuit models of ferroelectric device," *Journal of computational electronics*, vol. 16, pp. 1236–1256, 8 2017.
- [11] T. Kim, J. A. del Alamo, and D. A. Antoniadis, "Dynamics of HfZrO<sub>2</sub> Ferroelectric Structures: Experiments and Models," in 2020 IEEE International Electron Devices Meeting (IEDM), pp. 21.4.1–21.4.4, 2020.
- [12] C. Alessandri, P. Pandey, and A. C. Seabaugh, "Experimentally validated, predictive monte carlo modeling of ferroelectric dynamics and variability," in 2018 IEEE International Electron Devices Meeting (IEDM), pp. 16.2.1–16.2.4, 2018.
- [13] N. Feng, H. Li, C. Su, L. Zhang, Q. Huang, R. Wang, and R. Huang, "A dynamic compact model for ferroelectric capacitance," *IEEE electron device letters*, vol. 43, pp. 390–393, 3 2022.
- [14] Applied Materials, "Ginestra<sup>TM</sup> simulation software platform." Available: https://www.appliedmaterials.com/eu/en/semiconductor/solutions-and-software/software-solutions/ginestra-simulation-platform.html.
- [15] L. Fehlings, M. Hanif Ali, P. Gibertini, E. A. Gallicchio, U. Ganguly, V. Deshpande, and E. Covi, "Heracles: A hfo2 ferroelectric capacitor compact model for efficient circuit simulations," *IEEE Transactions on Electron Devices*, vol. 72, no. 11, pp. 6009–6014, 2025.
- [16] L. Larcher, A. Padovani, and P. Pavan, "Leakage current in hfo2 stacks: From physical to compact modeling," in *Nanotechnology 2012: Electronics, Devices, Fabrication, MEMS, Fluidics and Computational*, pp. 809–814, NSTI, 2012.
- [17] L. Vandelli, A. Padovani, L. Larcher, R. Southwick, W. Knowlton, and G. Bersuker, "A physical model of the temperature dependence of the current through sio2/hfo2 stacks," *IEEE Transactions on Electron Devices*, vol. 58, no. 9, pp. 2878–2887, 2011.